

CONSTRAINTS ON FUNDAMENTAL COSMOLOGICAL PARAMETERS WITH UPCOMING REDSHIFTED 21 CM OBSERVATIONS

JUDD D. BOWMAN¹, MIGUEL F. MORALES², JACQUELINE N. HEWITT¹

Draft version November 10, 2018

ABSTRACT

Constraints on cosmological parameters from upcoming measurements with the Mileura Widefield Array—Low Frequency Demonstrator (MWA-LFD) of the redshifted 21 cm power spectrum are forecast assuming a flat Λ CDM cosmology and that the reionization of neutral hydrogen in the intergalactic medium occurs below a redshift of $z = 8$. We find that observations with the MWA-LFD cannot constrain the underlying cosmology in this scenario. In principle, a similar experiment with a 10-fold increase in collecting area could provide useful constraints on the slope of the inflationary power spectrum, n_s , and the running of the spectral index, α_s , but these constraints are subject to the caveat that even a small reionization contribution could be confused with the cosmological signal. In addition to the redshifted 21 cm signal, we include two nuisance components in our analysis related to the systematics and astrophysical foregrounds present in low-frequency radio observations. These components are found to be well separated from the signal and contribute little uncertainty ($<30\%$) to the measured values of the cosmological model parameters.

Subject headings: Cosmology: Early Universe, Galaxies: Intergalactic Medium, Radio Lines: General, Techniques: Interferometric

1. INTRODUCTION

Hydrogen gas in the intergalactic medium (IGM) is a promising tool for studying some of the most interesting topics in astrophysics, including the nature of the first luminous objects, the processes of structure formation, and cosmology. Prior to the epoch of reionization (EOR), when radiation from the first luminous sources reionized the IGM, the 21 cm hyperfine line from neutral hydrogen is predicted to be visible against the cosmic microwave background (CMB) with relative brightness temperature of order ± 10 mK. At high redshifts, the spin temperature of HI is expected to be less than the CMB temperature, making the line visible in absorption, whereas at lower redshifts, after radiation from the first luminous objects has begun to heat the IGM but before it has reionized it, the line should be evident as emission.

As the primordial hydrogen cools following recombination and later reheats, density contrasts are revealed as fluctuations in the brightness temperature of the redshifted 21 cm line (Sunyaev & Zeldovich 1972; Hogan & Rees 1979; Scott & Rees 1990; Iliev et al. 2002, 2003; Loeb & Zaldarriaga 2004; Barkana & Loeb 2005b). At high redshifts, the power spectrum of these fluctuations is expected to follow closely the dark matter power spectrum and measurements from this epoch could, independently from CMB and galaxy clustering experiments, constrain cosmological models. At lower redshifts, as the first luminous objects ionize their surroundings, voids are expected to appear in the diffuse emission (Madau et al. 1997; Tozzi et al. 2000; Ciardi & Madau 2003; Zaldarriaga et al. 2004; Furlanetto et al. 2004). Measurements of the power spectrum during this epoch

would help reveal the characteristics of the first luminous objects.

Recent efforts have distinguished theoretical aspects of redshifted 21 cm observations that are particularly relevant for constraining cosmological models. Barkana & Loeb (2005c) discuss the ability of redshifted 21 cm observations to constrain the geometry of the high redshift universe between recombination and reionization; Ali et al. (2005) and Barkana & Loeb (2005a) have shown that differences in the line-of-sight versus angular components of a redshifted 21 cm power spectrum measurement can be used to separate primordial density perturbations from features caused by the radiative processes responsible for reionization; and Barkana (2006) has discussed the application of the Alcock-Paczynski (AP) test to redshifted 21 cm measurements. Additionally, Barkana & Loeb (2005b) consider the effects of the earliest galaxies on the redshifted 21 cm fluctuations and Naoz & Barkana (2005) discuss using redshifted 21 cm observations to study the thermal history of hydrogen gas by detecting a cutoff in the power spectrum due to thermal broadening of the line.

The experimental challenges of detecting and characterizing neutral hydrogen in the IGM at high redshift are significant. While reaching the sensitivity limit needed to detect the redshifted 21 cm radio background is readily achievable by very small experiments, statistical measurements of the fluctuation power spectrum require the collecting area of the much larger arrays—MWA-LFD, LOFAR, and PAST—currently under development (Bowman et al. 2006). Even after the required collecting areas have been reached, anticipated challenges remain. Astrophysical foreground contaminants are five orders of magnitude brighter than the redshifted 21 cm emission. Removing the foreground signatures from observations requires extremely precise observational calibration.

In this paper, we expand on earlier calculations of the

Electronic address: jdbowman@mit.edu

¹ MIT Kavli Institute for Astrophysics and Space Research, 77 Massachusetts Avenue, Cambridge, MA 02139, USA

² Harvard-Smithsonian Center for Astrophysics, 60 Garden Street, Cambridge, MA 02138, USA

sensitivity of the first generation arrays to forecast their ability to place constraints on cosmological models from measurements of the redshifted 21 cm power spectrum. In order to treat the best-case scenario and to simplify the analysis, we have chosen to assume that reionization has not yet begun by the target redshift range of $8 < z < 10$. This assumption represents the most optimistic scenario generally consistent with the existing evidence about when reionization began from quasar absorption line measurements (Djorgovski et al. 2001; Becker et al. 2001; Fan et al. 2003; Wyithe & Loeb 2004) and from Thomson scattering measurements by the WMAP satellite (Spergel et al. 2006). These measurements suggest reionization occurred at redshifts $z \gtrsim 6$ and $z \sim 10$, respectively.

We begin in Section 2 by reviewing the observational process of measuring the highly redshifted 21 cm power spectrum and describing the fiducial experiments. In Section 3, the method to forecast constraints on cosmological parameters is described in terms of statistical errors using a Fisher matrix treatment of the full three-dimensional power spectrum. The calculation marginalizes over several cosmological parameters and two anticipated contributions related to the astrophysical foreground contaminants. The results are discussed in Section 4 and encapsulated in Figure 2.

A similar study has been performed in parallel by McQuinn et al. (2006). While we analyze the characteristics relevant to constraining cosmological models with the initial generation of experiments and in the presence of two nuisance contributions, their analysis explores the benefit of combining redshifted 21 cm measurements with information from other experiments, such as WMAP and Planck. Together, the two efforts provide a thorough overview of the potential of future redshifted 21 cm power spectrum measurements to contribute to cosmology.

2. THE MEASUREMENT

The basis of the statistical measurement of the redshifted 21 cm power spectrum using low-frequency, wide-field radio observations has been developed in the literature by Morales & Hewitt (2004), Zaldarriaga et al. (2004), Morales (2005), and Bowman et al. (2006). These efforts are built on the similar approach employed for interferometric measurements of CMB anisotropies (White et al. 1999; Hobson & Maisinger 2002; Myers et al. 2003). Here, we review the relevant properties of the measurement; we direct the reader to the previous works for additional details.

Neutral hydrogen is optically thin to the 21 cm line. Thus, through the combination of their angular and spectral responses, the visibility measurements of low-frequency radio arrays inherently sample the emission from a three-dimensional volume of space at high redshift (Morales & Hewitt 2004). The measurements may be represented in a fully Fourier domain and expressed in coordinates convenient for studying cosmology ($\mathbf{k} \equiv k_1, k_2, k_3$) or in coordinates more directly related to instrumental considerations (u, v, η).

The fluctuation power spectrum of redshifted 21 cm emission in the sampled volume of space is mapped to an instrumental response by the convolution of the power spectrum, $P_{HI}(\mathbf{k})$, with the instrumental window func-

tion, $W(\mathbf{k})$, according to (Morales & Hewitt 2004)

$$C^{HI}(\mathbf{k}) = \langle |\Delta I(\mathbf{k})|^2 \rangle = \int P_{HI}(\mathbf{k}) |W(\mathbf{k} - \mathbf{k}')|^2 d^3k', \quad (1)$$

where the window function is given by the Fourier transform of the instruments angular and frequency response, and is very sharply peaked for the cases we will consider (see Section 2.2).

There is an inherent uncertainty in the measurement of the redshifted 21 cm power spectrum from cosmic sample variance. The uncertainty can be estimated by dividing the observed three-dimensional Fourier space into a large number of independent cells, where the volume of each cell is approximately the size of the window function, $W(\mathbf{k})$. For the regime of interest in our calculations, the variance in the measured power spectrum is then $C_{ij}^V(\mathbf{k}) \approx C^{HI}(\mathbf{k}) \delta_{ij}$, where the indices i and j run over all the independent cells in the sampled volume.

2.1. Contributions from Astrophysical Foregrounds

The redshifted 21 cm emission is not the only source of power in low-frequency radio observations. Astrophysical foregrounds are several orders of magnitude stronger and dominate the measured signal. The foregrounds include free-free and synchrotron emission from the Galaxy, extragalactic point sources, and free-free emission from elections in the IGM.

The bright foregrounds manifest themselves in several ways. First, the Galactic emission dominates the thermal noise in the measurements, especially at lower frequencies. Although much of this large-scale emission is expected to be resolved-out by interferometric observations, its effect on antenna temperature remains.

The contribution to the measured power spectrum due to thermal noise is substantial, but white ($\langle C^N(\mathbf{k}) \rangle = \text{constant}$), and therefore should be readily removed. In our calculations, we will assume that it has been removed (but allow for an imperfect subtraction by including an offset parameter in the model). After this subtraction, the thermal uncertainty per independent cell in the three-dimensional measured power spectrum can be approximated, in instrumental coordinates, using (Morales 2005, His Eqn. 11)

$$[C_{ij}^N(\mathbf{u})]_{\text{rms}} = 2 \left(\frac{2k_B T_{sys}}{\epsilon dA d\eta} \right)^2 \frac{1}{B \bar{n}(\mathbf{u}) t} \delta_{ij}, \quad (2)$$

where dA is the physical antenna area, $d\eta$ is the inverse of the total bandwidth, k_B is Boltzmann's constant, T_{sys} is the total system temperature, ϵ is the efficiency, B is the total bandwidth, \bar{n} is the time average number of baselines in an observing cell, and t is the total observation time. This equation is derived from the corresponding relationship for interferometric measurements of CMB anisotropies in White et al. (1999, Their Eqn. 16). Although the measured power spectrum in this case is three-dimensional, the parameters in Equation 2 are approximately independent of frequency within the observing band. The thermal uncertainty per independent cell, therefore, is taken also to be independent of η (and k_3). Additionally, for the MWA-LFD, the time-averaged visibility distributions are expected to be dense and to

have nearly circular symmetry, thus $\bar{n}(\mathbf{u})$ depends only on $\sqrt{u^2 + v^2}$.

The second important effect of astrophysical foregrounds is that they produce their own signatures in the measured power spectrum. The dominant foreground signature is expected to be due to extragalactic (and Galactic) point sources, which introduces a distinct component in the observations that is very bright (ranging up to ~ 1000 K for individual sources) and highly structured on the sky. Fortunately, these foreground contaminants are expected to be distinct from the redshifted 21 cm signal in their angular correlation functions and in their frequency behavior; and recent studies indicate that statistical techniques should provide methods to separate them from the desired signal (Oh & Mack 2003; Di Matteo et al. 2004; Zaldarriaga et al. 2004; Morales & Hewitt 2004; Santos et al. 2005; Wang et al. 2006; Morales et al. 2005).

We will assume that the foregrounds have been cleaned from the measured signal. Even the best subtraction algorithms leave residual traces of the contaminant, however, and a perfect model may produce an imperfect subtraction simply due to thermal uncertainty in the measurement. Such a subtraction error would result in a power spectrum signature following the shapes of the model components (Morales et al. 2005). The principle residual signature due to this kind of subtraction error for extragalactic point sources can be quantified as a k_3 -dependent factor, $C^F(k_3) \propto k_3^{-2}$. Since extragalactic point sources are expected to be the most significant astrophysical foreground contaminant we include this contribution in our analysis as a nuisance term.

2.2. Reference Experiments

The selection of reference experiments is critical to the outcome of the forecasting calculations since the uncertainties in redshifted 21 cm power spectrum measurements are coupled very closely to instrument design. The first generation of low-frequency radio arrays developed to perform redshifted 21 cm measurements includes three experiments: the Low Frequency Array³ (LOFAR) being constructed in the Netherlands, the Primeval Structure Telescope⁴ (PAST) under development in northwestern China, and the MWA-LFD⁵ in western Australia. The designs of these instruments reflect different priorities and different approaches, but they all result in similar predicted sensitivities for measurements of the redshifted 21 cm power spectrum. For example, although LOFAR will have the largest total collecting area (by a factor of ~ 10), its planned antenna distribution scheme is better suited for imaging applications than power spectrum measurements and its sensitivity is consequently lessened. The design of the MWA-LFD, on the other hand, has been optimized for power spectrum measurements and exploits the wide fields-of-view that are inherent in dipole-based systems to overcome its more limited collecting area.

Because of its focus on measurements of the redshifted 21 cm power spectrum, we have chosen to base the design of the reference experiments in our calculations on the

³ <http://www.lofar.org>

⁴ Pen et al. (2004)

⁵ <http://haystack.mit.edu/ast/arrays/mwa>

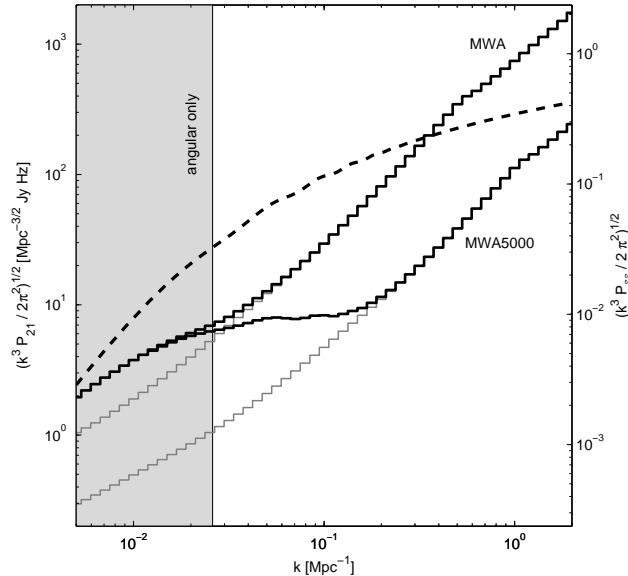


FIG. 1.— Uncertainties (stepped lines) in spherically averaged power spectrum measurements due to thermal and cosmic sample variance for a single $\Delta z \simeq 0.5$ (8 MHz) region at redshift $z = 8$ observed by the MWA and MWA5000 reference experiments relative to the fiducial, redshifted 21 cm power spectrum (dashed line). The thermal uncertainty (thin gray lines) is overshadowed by uncertainty due to cosmic sample variance at large scales (small k). The combined uncertainty is shown as black lines. Due to the limited redshift range over which cosmic evolution can be neglected ($\Delta z \simeq 0.5$), the measurements in the light-gray region to the left of the vertical line are constrained only by angular fluctuations and will thus be most affected by astrophysical foreground contamination. The predicted constraints on the cosmological model parameters in Figure 2 and Tables 5 and 6 were derived using the full three-dimensional power spectrum, and thus, this plot of the uncertainty in the spherically averaged measurement is best used as a guide to illustrate which scale sizes will be most important in the constraints.

MWA-LFD. We will consider two experiments. The first is identical to the fiducial MWA-LFD design described in Bowman et al. (2006, Their Section 2). The array design consists of $N = 500$ antennas distributed within a $D = 1500$ m diameter circle. The density of antennas as a function of radius is taken to go as $\sim r^{-2}$, but capped at a maximum density of one antenna per 18 m^2 . The antenna response is approximated by

$$W(\theta) = \cos^2\left(\frac{\pi}{2}\theta/\Theta\right), \quad \theta < \Theta \quad (3)$$

where Θ is proportional to wavelength and spans from 31 to 38° over the range of interest. The angular resolution of the array is given by λ/D and the total collecting area by $N dA$, where dA is the collecting area of each antenna and scales like $dA = 16(\lambda^2/4)$ for $\lambda < 2.1$ m and is capped for longer wavelengths. Finally, the full bandwidth of the instrument is $B = 32$ MHz and the frequency resolution is 8 kHz. All of the fiducial properties are summarized in Tables 1 and 2.

For the analysis in this paper, we define the observation to be of a single field with 1000 hours integration during the most favorable circumstances. Additionally, we set the frequency coverage to $125 < f < 157$ MHz, which spans $10 > z > 8$, and treat the bandwidth as four consecutive 8 MHz regions, each of which spans approximately $\Delta z = 0.5$. In principle, the observed 21 cm power spectrum is varying continuously with redshift due

to cosmology-dependent effects. By dividing our measured volume of space into thin regions in redshift we may ignore cosmic evolution within each region.

The second reference experiment is based on an expanded MWA-LFD configuration similar to the one considered by Wyithe et al. (2005), although more condensed. Dubbed the MWA5000, the expanded array contains 5000 antennas distributed over a 3000 m diameter region. The density of antennas remains $\sim r^{-2}$ and capped at one per 18 m². The antenna response, instrument bandwidth, and frequency resolution are also unchanged (see Tables 1 and 2). In both experiments all antenna elements are correlated to preserve the large field of view.

Figure 1 illustrates the relative sensitivities of the two reference experiments by plotting their uncertainties in spherically averaged bins due to thermal noise and cosmic sample variance along with a fiducial, redshifted 21 cm power spectrum. The two reference experiments share a common level of uncertainty at large spatial scales (small k) due to cosmic sample variance since their fields of view are identical. At smaller spatial scales ($k \gtrsim 0.1$), however, the larger collecting area of the MWA5000 reduces its thermal uncertainty in a given integration time compared to that of the MWA. The MWA5000 is nearly an order of magnitude more sensitivity than the MWA at these scales.

3. METHOD

The Fisher information matrix provides a convenient method for translating uncertainties in power spectrum measurements to constraints on cosmological parameters (Tegmark et al. 1997). The minimum errors are calculated using the Fisher matrix:

$$F_{ab} = \sum_i \frac{1}{\sigma(\mathbf{k}_i)^2} \frac{\partial P(\mathbf{k}_i)}{\partial p_a} \frac{\partial P(\mathbf{k}_i)}{\partial p_b}, \quad (4)$$

where $\sigma^2 \equiv \sigma_N^2 + \sigma_V^2$ is the combined uncertainty per independent cell due to thermal noise and cosmic sample variance, P is the measured power in a cell given by Equation 5, and p is the set of model parameters. Taking the square roots of the diagonal elements of the inverse of Fisher matrix gives the errors.

The model we use for the observed power spectrum represents the measurement after substantial data reduction has occurred, including instrumental calibration and astrophysical foreground subtraction. At this stage, the observed power spectrum is parameterized based on three contributions:

$$P(\mathbf{k}) \equiv P_{HI}(k) + P_F(k_3) + P_N, \quad (5)$$

where the first term is the redshifted 21 cm contribution, the second is the primary residual astrophysical (extragalactic point source) foreground contribution discussed in Section 2.1, and the third is the residual white thermal noise contribution (also discussed in Section 2.1).

For our assumption that reionization has heated the neutral hydrogen in the IGM but not yet produced significant features in the emission patterns of the gas by the target redshifts, the redshifted 21 cm contribution to the model power spectrum follows the matter power spectrum and can be expressed at a given redshift as

$$P_{HI}(k) \equiv C_{Jy}^2 P_{\delta\delta}(k | A, \Omega_M, \Omega_b, h, n_s, \alpha_s), \quad (6)$$

where C_{Jy} is the strength of the 21 cm emission from mean-density neutral hydrogen gas in the IGM and $P_{\delta\delta}(\mathbf{k})$ is the matter power spectrum. At the target redshifts, fluctuations in the matter density are expected generally to be in the linear regime over the range of spatial scales sampled. For redshift $z = 8$, the perturbations at the smallest scales constrained by the measurements ($k \simeq 1 \text{ Mpc}^{-1}$) will be approximately 40%; and at the largest scales ($k \simeq 0.01 \text{ Mpc}^{-1}$), the perturbations will be less than 1%. In contrast to measurements of the matter power spectrum through large scale structure surveys of galaxies, redshifted 21 cm measurements probe directly the baryon density perturbations in the IGM, which follow closely the dark matter density perturbations. The effect of small deviations from the purely linear regime can be modeled easily in this case and we omit, therefore, this complication in our analysis. We use six parameters, $p = \{A, \Omega_M, \Omega_b, h, n_s, \alpha_s\}$, to describe the matter power spectrum. These parameters are summarized in Table 3 along with their fiducial values. Additionally, we constrain $\Omega_K = 0$ and $\Omega_\Lambda = 1 - \Omega_M$. To compute the matter power spectrum, we use CMBFAST (Seljak & Zaldarriaga 1996) and do not include velocity distortions or deviations from linear dynamics in the model.

As described in Section 2.1, the primary residual foreground contribution is a function of k_3 and is expressed as

$$P_F(k_3) \equiv F \times c_{norm} \left(\frac{k_3}{k_{norm}} \right)^{-2}, \quad (7)$$

where F is an amplitude scale factor of order unity and c_{norm} is a normalization constant. The thermal offset contribution does not vary with \mathbf{k} and is defined as

$$P_N \equiv N \times c_{norm}, \quad (8)$$

where N is also an amplitude scale factor of order unity. For the Fisher matrix analysis, both P_F and P_N are normalized by setting $k_{norm} = 0.01 \text{ Mpc}^{-1}$ and evaluating $c_{norm} = P_{HI}(k_{norm})$ at redshift $z = 8$. Thus, the magnitudes of F and N give the amplitudes of the residual contributions approximately relative to the peak value of the redshifted 21 cm power spectrum. Adding F and N to the set of six cosmological parameters yields the eight parameters, $p = \{A, \Omega_M, \Omega_b, h, n_s, \alpha_s, F, N\}$, which constitute the complete set of free variables of our base model.

4. RESULTS

The results of performing the Fisher matrix calculations for the two reference experiments described in Section 2.2 are summarized in Table 4, which lists the forecasted $1\text{-}\sigma$ uncertainties on the model parameters. These values indicate that observations with the MWA-LFD would not constrain the cosmological parameters significantly. The only exception to this finding is for α_s , which could be constrained to 0 ± 0.04 under the favorable assumptions used in the model. The second reference experiment, MWA5000, does constrain reasonably all the model parameters. Table 4 shows that this reference experiment provides constraints at levels approximately equivalent to those from the first-year WMAP results (Spergel et al. 2003, Their Table 10).

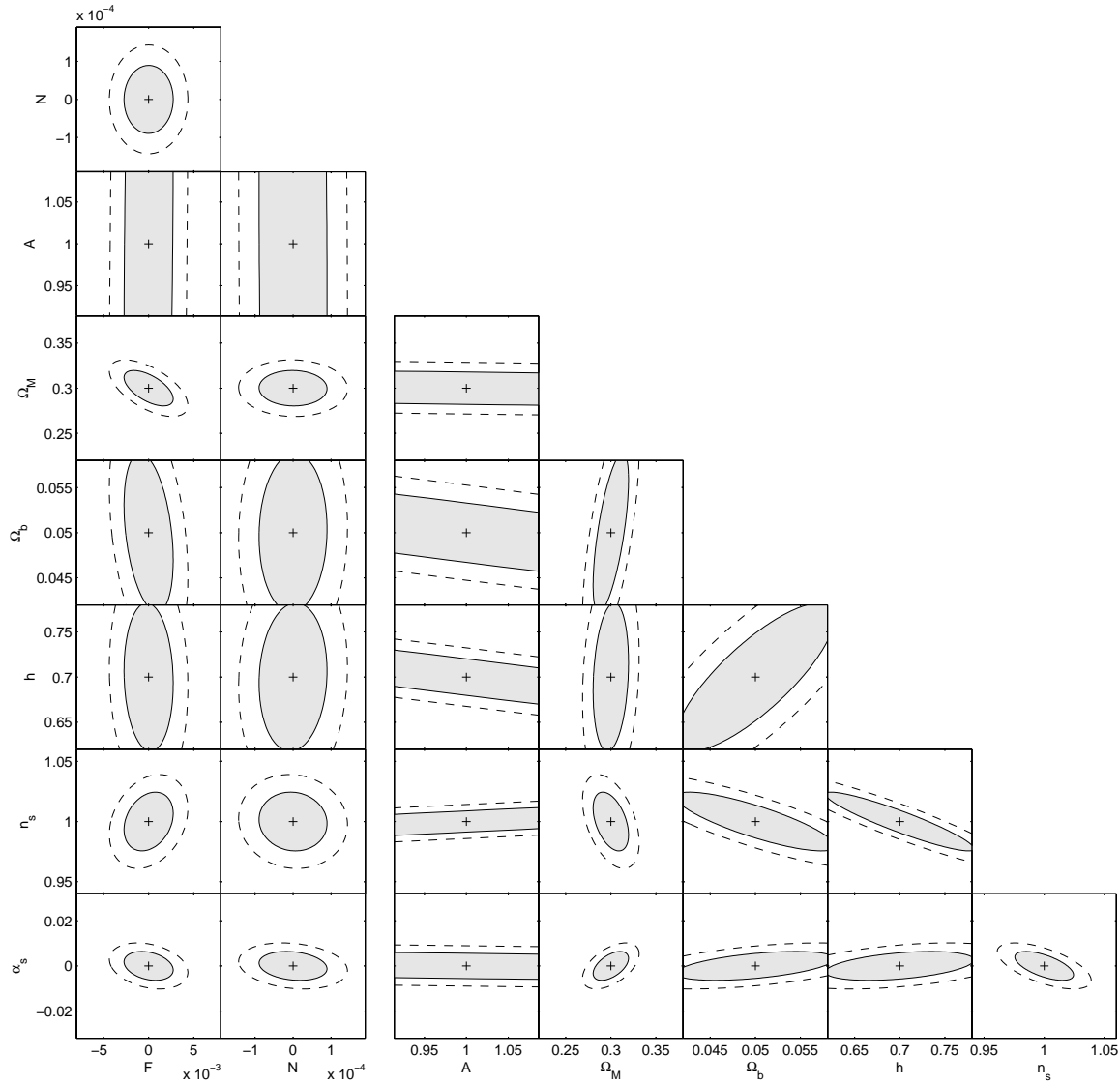


FIG. 2.— Marginalized elliptical error regions for pairs of model parameters for the MWA5000 reference experiment. The contours are for 68% (solid) and 95% (dashed) likelihood. The first two columns are set apart to emphasize the distinction between the nuisance components in the model due to astrophysical foregrounds and the cosmological terms. The bounds of the plotted regions for the cosmological parameters are set at twice the uncertainties ($\pm 2\sigma$) reported in the WMAP first-year results for the respective parameters. Thus, if the dotted ellipse is visible in a particular plot, the constraints on the parameters would be an improvement over WMAP. It is evident that the MWA5000 would do a relatively good job of constraining Ω_M , n_s , and α_s , and a comparatively poor job of constraining Ω_b and h . The inability of the MWA5000 to constrain the scalar amplitude, A , of the power spectrum is due to degeneracies with other parameters, in particular Ω_b and h , but also n_s .

The elements of the covariance matrices for each reference experiment are given in Tables 5 and 6, and additional information about the forecasted constraints for the MWA5000 is provided in Figure 2, which shows marginalized error ellipses for two-parameter combinations of the model parameters. The properties of these results are discussed in detail in the remainder of this section.

4.1. Parameter Dependencies

To facilitate a conceptual understanding of the origin of the constraints on the model parameters, it is instructive to individually vary the cosmological parameters and compare the resulting redshifted 21 cm signals. On all but the largest length scales, the experimentally observed

power spectrum is well approximated by

$$P_{\text{HI}}(u, v, \eta) \cong W^2 C_{\text{Jy}}^2 \left\{ P_{\delta\delta}(\mathbf{k}) \frac{d^3\mathbf{k}}{dudvd\eta} \right\}, \quad (9)$$

where W is the integrated value of the observational window function and represents the signal strength for a given instrument, and $d^3\mathbf{k}/dudvd\eta$ is the Jacobian for converting the units of the matter power spectrum to the observed units. The relationships between u, v, η and \mathbf{k} are (Morales & Hewitt 2004):

$$[k_1, k_2] = \frac{2\pi}{D_M(z)} [u, v] \quad (10)$$

$$k_3 \approx \frac{2\pi\nu_{21}H_0E(z)}{c(1+z)2} \eta, \quad (11)$$

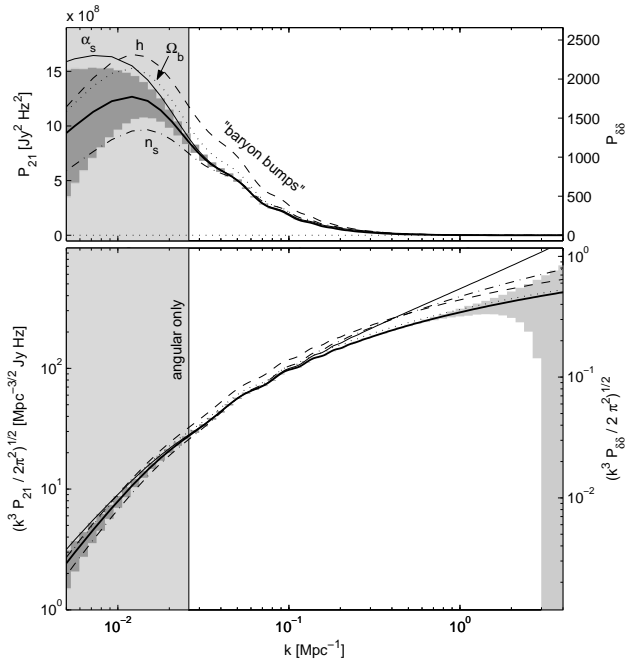


FIG. 3.— Redshifted 21 cm power spectrum for the fiducial cosmological model parameters, shown with four example variations of the parameter values. The top and bottom panels show the same elements plotted in different units. The thick solid line is for the fiducial model with standard cosmological parameters ($\Omega_b = 0.05$, $\Omega_M = 0.30$, $h = 0.70$, $n_s = 1.00$, $\alpha_s = 0$). The other curves are produced by adjusting one cosmological parameter from the fiducial: $\Omega_b + 10\%$ (dotted), $h + 10\%$ (dash), $n_s + 10\%$ (dash dot), and $\alpha_s = 0.1$ (thin solid). The dark shaded region indicates the $1\text{-}\sigma$ uncertainty due to cosmic variance within the observed field and the light shaded region (at large k) is the thermal uncertainty for the MWA5000 reference experiment. As in Figure 1, the measurements to the left of the vertical line are constrained by angular fluctuations only and will be most sensitive to astrophysical foreground contamination.

where

$$E(z) \equiv \sqrt{\Omega_M(1+z)^3 + \Omega_k(1+z)^2 + \Omega_\Lambda(1+z)^{3(1+w)}}, \quad (12)$$

and $D_M(z)$ and $\nu_{21} = 1420.4$ MHz are the transverse comoving distance and the rest-frame frequency of the hyperfine line, respectively.

In Equation 9, there are three separate contributions which may be affected by changing the cosmological parameters: the matter power spectrum itself, the neutral hydrogen emission factor, and the coordinate mapping between \mathbf{k} and u, v, η . The mapping between \mathbf{k} and u, v, η produces two effects when measuring the power spectrum. First, the region in u, v and η occupied by the observed power spectrum depends on the cosmological model. This effect is analogous to the observed CMB power spectrum shifting in ℓ for different cosmological models, but since the redshifted 21 signal is three-dimensional, there may be a difference in scaling between the sky-plane and line-of-sight dimensions. This additional degree of freedom gives rise to the AP test (Alcock & Paczynski 1979) (see also Seo & Eisenstein (2003) for an applicable discussion of constraining dark energy using baryon acoustic oscillations in power spectra from three-dimensional galaxy redshift surveys).

The second effect of coordinate mapping in the ob-

served power spectrum is the presence of a significant cosmology-dependent amplitude factor in the measured power spectrum due to the Jacobian contribution in Equation 9. Differentiating and combining Equations 10 and 11 yields the Jacobian:

$$\frac{d^3\mathbf{k}}{dudvd\eta} = \frac{(2\pi)^3 \nu_{21} H_0 E(z)}{c(1+z)^2 D_M^2(z)}. \quad (13)$$

The effect of the Jacobian amplitude factor is further compounded by the hydrogen emission factor, C_{Jy} . This term is unique to redshifted 21 cm experiments and provides a significant boost to the cosmology-dependent amplitude factor. Assuming the spin temperature of the neutral hydrogen in the IGM is significantly warmer than the CMB, the hydrogen emission factor goes as (Morales & Hewitt 2004, Their Equation 13 and Their Appendix A)

$$C_{Jy} \propto \frac{\Omega_b h}{E(z)} \bar{x}_{\text{HI}}, \quad (14)$$

where \bar{x}_{HI} is the mean neutral fraction (taken to be unity in this paper). Using Equations 13 and 14 and recalling that $D_M(z) \propto h^{-1}$, the amplitude of the observed power spectrum is now seen to be proportional to

$$P_{\text{HI}} \propto \frac{\Omega_b^2 h^5}{(1+z)^2 E(z)} P_{\delta\delta}. \quad (15)$$

Equation 15 indicates that the amplitude of the redshifted 21 cm fluctuations does contain useful information about the cosmological model (with the caveat that the HI spin temperature must be known). This is in contrast to measurements of the matter power spectrum by galaxy clustering surveys, where the connection between the observed amplitude of the power spectrum and the underlying physical amplitude remains weakly understood.

Figure 3 shows the spherically-binned redshifted 21 cm power spectrum signal for the fiducial model (thick line, $\Omega_b = 0.05$, $\Omega_M = 0.30$, $h = 0.70$, $n_s = 1.00$, $\alpha_s = 0$) along with the expected signals obtained by varying individual parameters. We can see that varying Ω_b or h primarily results primarily in a simple scaling of the observed power spectrum, as expected from Equation 15. Thus these parameters are highly degenerate with each other and with the amplitude factor A , as shown in Figure 2 and Table 6.

The primordial power spectrum slope n_s and running of the spectral index α_s do not enter into the overall amplitude factor in Equation 15 for the observed power spectrum, but instead affect the shape of the underlying matter power spectrum. Increasing n_s lowers the power at small k and increases the power at large k , whereas increasing α_s boosts the power spectrum at both extremes. Because these parameters do not strongly affect the amplitude normalization, they are relatively independent of A , Ω_b , and h as shown in Figure 2 and Table 6. They are also independent of our foreground parameter, F , because the shape they introduce is different than the k_3^{-2} shape of the residual foreground contamination. Thus n_s and α_s are the best constrained cosmological parameters for the planned redshifted 21 cm observations.

The last class of observational effects due to the cosmological model is from the coordinate mapping. Most significantly, for an increase in h , a radially inward shift of scales (see Equations 10 and 11, with $D_M(z) \propto h^{-1}$) counteracts the amplitude increase from the C_{Jy} and Jacobian factors over much of the observed range in k -space. Increasing Ω_M also shifts scales inward (through $E(z)$ and $D_M(z)$), but does so differently for the line-of-sight direction and the transverse directions. This AP effect cannot be represented easily in Figure 3, however, we have included it in all the constraints. The significance of the effect is limited since we take $\Omega_\Lambda = 1 - \Omega_M$. A 10% increase in Ω_M yields an approximately 4% reduction in scale, but only about 1% distortion between the directions. In general, coordinate based effects may be better constrained with observations targeting the quasar bubbles during reionization since sharper spatial features in the power spectrum may emerge during reionization due to characteristic sizes of reionized regions and Stromgren spheres around quasars.

4.2. Degeneracies in Amplitude

The uncertainty in A is considerable. Table 4 shows that the MWA5000 only constrains A to within 45%. The origin of this uncertainty is explained by the amplitude factor discussed above and is clearly evident in Table 6, which displays the large degeneracies (as normalized covariance factors with magnitudes close to unity) between A , Ω_b , h , and more unexpectedly, n_s . The degeneracy with n_s is due to the range of scales to which the experiments are sensitive, which is primarily after the pivot point for the primordial power spectrum spectral index ($k = 0.05 \text{ Mpc}^{-1}$). Therefore, changes in n_s tend to appear less similar to tilting to the power spectrum and more like changing the amplitude, although n_s remains well constrained. Additionally, the covariance between A and Ω_b confirms that the baryon acoustic oscillations in the power spectrum are not contributing much information about the baryon density relative to the amplitude changes from the C_{Jy} and Jacobian factors.

4.3. Residual Foreground Contamination

Mitigating astrophysical foreground contamination is an important issue for redshifted 21 cm experiments, whether attempting to constrain cosmological models or determine reionization processes and scenarios. To this end, the relationships between P_{HI} , P_F , and P_N , as described by the covariance between our model parameters A , F , and N are very useful to study in some detail.

The constraints on the amplitudes of the residual astrophysical foreground and residual thermal offset terms are especially encouraging. Neither contribution is significantly degenerate with changes to the redshifted 21 cm power spectrum. In particular, the long, diminishing tail of the redshifted 21 cm power spectrum provides many statistical samples which contribute little to knowledge of the cosmological parameters, yet provide good references to prevent degeneracy with changes in the magnitude of the residual thermal offset. Thus, P_N is constrained to better than 2% of the peak value of P_{HI} for the MWA-LFD and to better than 0.01% for the MWA5000.

As discussed in Section 2.1, the residual foreground contamination is expected to be a power-law along the

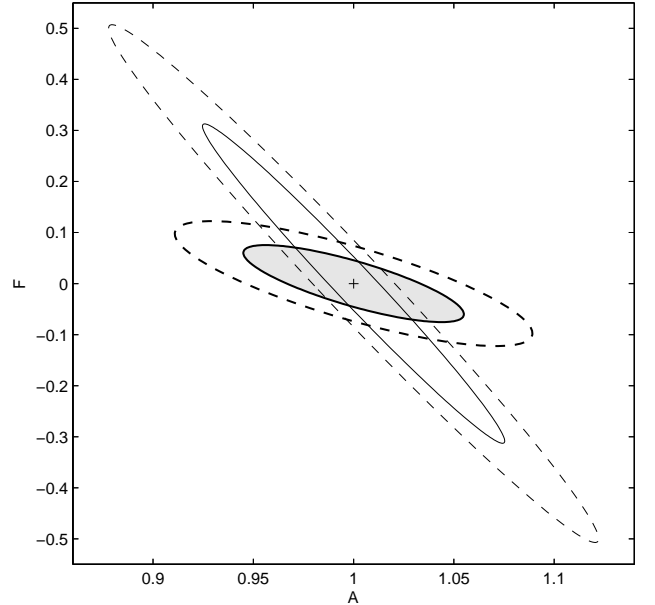


FIG. 4.— Unmarginalized error ellipses for the amplitudes of the redshifted 21 cm power spectrum and primary residual foreground contamination, A and F , forecasted for the MWA-LFD. The thick curves are for a Fisher matrix calculation utilizing the full three-dimensional measured power spectrum, while the thin curves are for the same calculation using spherical bins in k -space. The contours are for 68% and 95% likelihood. The behavior is similar for the MWA5000, although the errors are smaller.

line-of-sight direction and to have little structure in the transverse directions. This is distinct from the redshifted 21 cm power spectrum with its generally spherical symmetry, although geometrical effects due to the shape of the observed volume of space work to negate this distinction. The observed region has dimensions of ~ 9000 by ~ 9000 Mpc in the sky-plane, but only ~ 100 Mpc along the line-of-sight (Bowman et al. 2006). Since all three dimensions are sampled with an approximately equal number of divisions, this flattened shape is inverted when transforming into k -space, leading to a highly elongated data cube in the k_3 -direction. For the MWA-LFD, the maximum k in the sky-plane (k_1, k_2) is approximately 0.05 Mpc^{-1} , while along k_3 it is over 10 Mpc^{-1} . Therefore, much of the information in the measurement about the redshifted 21 cm power spectrum is actually coming from the line-of-sight direction. Furthermore, the lack of depth in the observed volume prevents the experiments from probing large scales in the line-of-sight direction and, thus, the peak of the power spectrum (at $k \approx 0.01$) is not well constrained. This means that not only is most of the information coming from the line-of-sight direction, it is coming from the power law-like tail ($\sim k^{-3}$) of the power spectrum. These effects combine to make the redshifted 21 cm contribution and residual foreground contamination less distinguishable in the measured power spectrum.

Fortunately, the analysis indicates that the residual foreground component is well separated from the redshifted 21 cm power spectrum and does not affect substantially the ability to constrain the cosmological parameters. From Table 6 and Figure 2, we see that the largest degeneracy is between F and Ω_M . Removing P_F

from the model power spectrum, and thus F from the parameter set such that $p = \{A, \Omega_M, \Omega_b, h, n_s, \alpha_s, N\}$, would reduce the forecasted uncertainty on Ω_M by less than 30% in an observation with MWA5000. The contributions from the residual thermal offset, P_N , are even less.

In our analysis so far we have treated the full three-dimensional measured power spectrum. This has maximized the effects of the symmetry differences between the 21 cm power spectrum and primary residual foreground power spectrum. We might have instead considered a reduced one-dimensional power spectrum produced by averaging over spherical bins in k -space. This approach is used commonly to reduce data in which the expected signal has approximately spherical symmetry.

In Figure 4, we compare the full three-dimensional treatment with the spherically-binned approach by plotting unmarginalized error ellipses in the A-F plane of parameter space for both cases. It is clear that the binned method produces a significantly larger degeneracy between the magnitude of the residual foreground contribution and the amplitude of the 21 cm neutral hydrogen power spectrum than the full three-dimensional treatment.

4.4. Dark Energy Equation of State

Determining the nature of dark energy has become an important goal in astrophysics and the applicability of future large-scale structure surveys to this topic has been considered recently with generally favorable results (Seo & Eisenstein 2003; Linder 2003; Hu & Haiman 2003; Wang et al. 2004; Abdalla & Rawlings 2005). With their similarities to large-scale structure surveys, would measurements of the redshifted 21 cm neutral hydrogen power spectrum also improve knowledge of dark energy?

Including the dark energy equation of state parameter, w , as a free variable in the Fisher matrix analysis, so that $p = \{A, \Omega_M, \Omega_b, h, n_s, \alpha_s, w, F, N\}$, yields little information about the nature of dark energy. Neither the MWA-LFD nor the MWA5000 are able to provide meaningful constraints on w without priors from other experiments. Furthermore, the constraints on Ω_M , Ω_b , and h are significantly weakened (by up to an order of magnitude), although information is retained about the primordial power spectrum.

Although the MWA5000 reference experiment would

be able to detect the baryon acoustic oscillations (see Figure 3), the experiment targets emission from high redshifts prior to the epoch of dark energy domination. The value of the experiment would be relevant only as an intermediate measurement between the CMB and low redshift large-scale structure surveys (Barkana 2006), but could be important if dark energy had unusual behavior at high redshifts.

5. CONCLUSION

The first generation of redshifted 21 cm experiments have been shown previously to have the potential to characterize the processes and history of reionization at redshifts $6 < z < 12$. In this effort, we have considered a scenario in which reionization is not the dominant contribution to the measured power spectrum during this period. Our findings demonstrate that the initial experiments would not contribute substantially to knowledge of the underlying cosmology under these circumstances. While they may provide some use to cosmological studies, the primary science return of the first generation of redshifted 21 cm experiments will be regarding the astrophysics of reionization.

Under the optimistic assumptions used in this paper, the second-generation experiments, similar to the MWA5000 reference experiment, will be better suited to constrain Ω_M and the primordial power spectrum through n_s and α_s . Even for the spectral index properties it is difficult to envision a scenario where redshifted 21 cm observations alone could provide an unambiguous constraint on cosmological information, however, since the signal could easily be confused if the universe had a small amount of reionization structure on small scales or spin temperature fluctuations in the IGM.

We have also considered the covariance between the redshifted 21 cm power spectrum due to a fully neutral IGM and the primary residual foregrounds of low-frequency radio observations. The signal and contamination components were easily distinguished in the full three-dimensional power spectrum analysis.

We would like to thank Matt McQuinn, Matias Zaldarriaga, Oliver Zahn, and Lloyd Knox for fruitful discussions. Support for this work was provided by NSF grant AST-0121164 and the MIT School of Science.

REFERENCES

- Abdalla, F. B., & Rawlings, S. 2005, MNRAS, 360, 27
 Alcock, C., & Paczynski, B. 1979, Nature, 281, 358
 Ali, S. S., Bharadwaj, S., & Pandey, B. 2005, MNRAS, 363, 251
 Barkana, R. 2006, MNRAS, submitted
 Barkana, R., & Loeb, A. 2005a, ApJ, 624, L65
 Barkana, R., & Loeb, A. 2005b, ApJ, 626, 1
 Barkana, R., & Loeb, A. 2005c, MNRAS, 363, L36
 Becker, R. H., et al. 2001, AJ, 122, 2850
 Bowman, J. D., Morales, M. F., & Hewitt, J. N. 2006, ApJ, 638, 20
 Ciardi, B., & Madau, P. 2003, ApJ, 596, 1
 Di Matteo, T., Ciardi, B., & Miniati, F. 2004, MNRAS, 355, 1053
 Djorgovski, S. G., Castro, S., Stern, D., & Mahabal, A. A. 2001, ApJ, 560, L5
 Fan, X., et al. 2003, AJ, 125, 1649
 Furlanetto, S. R., Zaldarriaga, M., & Hernquist, L. 2004, ApJ, 613, 16
 Hobson, M. P., & Masinger, K. 2002, MNRAS, 334, 569
 Hogan, C. J., & Rees, M. J. 1979, MNRAS, 188, 791
 Hu, W., & Haiman, Z. 2003, Phys. Rev. D, 68, 063004
 Iliev, I. T., Scannapieco, E., Martel, H., & Shapiro, P. R. 2003, MNRAS, 341, 81
 Iliev, I. T., Shapiro, P. R., Ferrara, A., & Martel, H. 2002, ApJ, 572, L123
 Linder, E. V. 2003, Phys. Rev. D, 68, 083504
 Loeb, A., & Zaldarriaga, M. 2004, Physical Review Letters, 92, 211301
 Madau, P., Meiksin, A., & Rees, M. J. 1997, ApJ, 475, 429
 McQuinn, M., Zahn, O., Zaldarriaga, Z., Hernquist, L., & Furlanetto, S. 2006, ApJ, submitted
 Morales, M. F. 2005, ApJ, 619, 678
 Morales, M. F., Bowman, J. D., & Hewitt, J. N. 2005, ArXiv Astrophysics e-prints
 Morales, M. F., & Hewitt, J. 2004, ApJ, 615, 7

- Myers, S. T., et al. 2003, ApJ, 591, 575
Naoz, S., & Barkana, R. 2005, MNRAS, 362, 1047
Oh, S. P., & Mack, K. J. 2003, MNRAS, 346, 871
Pen, U. L., Wu, X. P., & Peterson, J. 2004, Ch.J.A.A., submitted
Santos, M. G., Cooray, A., & Knox, L. 2005, ApJ, 625, 575
Scott, D., & Rees, M. J. 1990, MNRAS, 247, 510
Seljak, U., & Zaldarriaga, M. 1996, ApJ, 469, 437
Seo, H.-J., & Eisenstein, D. J. 2003, ApJ, 598, 720
Spergel, D. N., et al. 2006, ArXiv Astrophysics e-prints
Spergel, D. N., et al. 2003, ApJS, 148, 175
Sunyaev, R. A., & Zeldovich, Y. B. 1972, A&A, 20, 189
Tegmark, M., et al. 2004, Phys. Rev. D, 69, 103501
Tegmark, M., Taylor, A. N., & Heavens, A. F. 1997, ApJ, 480, 22
Tozzi, P., Madau, P., Meiksin, A., & Rees, M. J. 2000, ApJ, 528, 597
Wang, S., Khoury, J., Haiman, Z., & May, M. 2004, Phys. Rev. D, 70, 123008
Wang, X., Tegmark, M., Santos, M., & Knox, L. 2006, Phys. Rev. D, submitted
White, M., Carlstrom, J. E., Dragovan, M., & Holzappel, W. L. 1999, ApJ, 514, 12
Wyithe, J. S. B., & Loeb, A. 2004, Nature, 427, 815
Wyithe, J. S. B., Loeb, A., & Barnes, D. G. 2005, ApJ, 634, 715
Zaldarriaga, M., Furlanetto, S. R., & Hernquist, L. 2004, ApJ, 608, 622

TABLE 1
FIDUCIAL OBSERVATION PARAMETERS

Parameter	MWA-LFD (MWA5000)
Array configuration, $\rho(r)$ (m^{-2})	$\sim r^{-2}$
Array diameter, D (m)	1500 (3000)
Bandwidth, B (MHz)	32
Frequency resolution (kHz)	8
Number of antennas, N	500 (5000)

NOTE. — Array parameters for the MWA-LFD and MWA5000 reference experiments.

TABLE 2
REDSHIFT DEPENDENT PARAMETERS

	$z = 8$	$z = 10$
Angular resolution ($^{\circ}$)	0.073 (0.036)	0.089 (0.044)
Antenna collecting area, dA (m^2)	14	18
Antenna response scale, Θ ($^{\circ}$)	31	38
Frequency (MHz)	158	129
System temperature, T_{sys} (K)	440	690

NOTE. — Characteristics of the fiducial observation that depend on frequency, and thus on redshift, are listed along with their values at the $z = 8$ and $z = 10$ edges of the observation redshift range. In the calculations, the values of the fiducial parameters at intermediate redshifts were linearly interpolated from the end points (except for Θ , see text). For the angular resolution, the MWA-LFD and MWA5000 have different properties due to the larger size of the MWA5000 (whose values are listed parenthetically).

TABLE 3
MODEL POWER SPECTRUM PARAMETRIZATION

Parameter	Symbol	Fiducial Value
Normalization (at $k = 0.05 \text{ Mpc}^{-1}$)	A	1.00
Matter density	Ω_M	0.30
Baryon density	Ω_b	0.05
Hubble constant	h	0.70
Scalar spectral index (at $k = 0.05 \text{ Mpc}^{-1}$)	n_s	1.00
Running index slope (at $k = 0.05 \text{ Mpc}^{-1}$)	$\alpha_s \equiv dn_s/d \ln k$	0.00
Residual foreground amplitude	F	0.00
Residual thermal offset	N	0.00

NOTE. — Eight parameters used to describe the measured power spectrum, and their values for the fiducial model. The first six rows give the basic parameters used to describe the matter power spectrum and the last two rows give the parameters to quantify the residual astrophysical foreground and residual thermal offset terms.

TABLE 4
FORECASTED UNCERTAINTIES FOR THE MODEL PARAMETERS

	A	F	D	Ω_M	Ω_b	h	n_s	α_s
	1.00	0.00	0.00	0.30	0.05	0.70	1.00	0.00
MWA-LFD	6.69	0.09	2e-3	0.21	0.07	0.88	0.2	0.04
MWA5000	0.45	2e-3	1e-4	0.01	6e-3	0.05	0.02	4e-3
WMAP	0.09	—	—	0.04	4e-3	0.04	0.03	0.02
SDSS	0.10	—	—	0.05	2e-3	0.04	0.03	—

NOTE. — Forecasted $1\text{-}\sigma$ uncertainties for the model parameters. The first row gives the fiducial values for reference. The MWA-LFD reference experiment does not significantly constrain cosmological parameters, while the MWA5000 does a reasonably good of job, particularly for Ω_M and the primordial power spectrum spectral index descriptors, n_s and α_s . For comparison, the last two rows display approximate constraints for similar models from WMAP (Spergel et al. 2003, Their Table 10) and SDSS (Tegmark et al. 2004, Their Table 3).

TABLE 5
COVARIANCE MATRIX FOR MWA-LFD

	A	F	D	Ω_M	Ω_b	h	n_s	α_s
A	1.00							
F	-0.09	1.00						
D	-0.09	0.01	1.00					
Ω_M	-0.04	-0.72	-0.04	1.00				
Ω_b	-0.87	-0.24	0.04	0.49	1.00			
h	-0.97	0.24	0.11	-0.20	0.72	1.00		
n_s	0.95	0.04	-0.15	-0.12	-0.82	-0.92	1.00	
α_s	-0.41	-0.37	-0.15	0.63	0.69	0.23	-0.32	1.00

NOTE. — Elements of the covariance matrix for the MWA-LFD calculated by taking the inverse of the Fisher matrix, F . Each element has been normalized according to $c_{ab}/\sqrt{c_{aa}c_{bb}}$, where the diagonal elements are the squares of the $1\text{-}\sigma$ uncertainties given in Table 4.

TABLE 6
COVARIANCE MATRIX FOR MWA5000

	A	F	D	Ω_M	Ω_b	h	n_s	α_s
A	1.00							
F	0.20	1.00						
D	-0.07	0.00	1.00					
Ω_M	-0.40	-0.60	-0.02	1.00				
Ω_b	-0.93	-0.35	0.05	0.66	1.00			
h	-0.97	-0.08	0.08	0.19	0.81	1.00		
n_s	0.93	0.27	-0.07	-0.46	-0.83	-0.92	1.00	
α_s	-0.48	-0.28	-0.20	0.53	0.50	0.42	-0.62	1.00

NOTE. — Same as Table 3, but for the MWA5000.